Applied Catalysis B: Environmental 328 (2023) 122493

Contents lists available at ScienceDirect

Applied Catalysis B: Environmental

journal homepage: www.elsevier.com/locate/apcatb

In situ cascade growth-induced strong coupling effect toward efficient photocatalytic hydrogen evolution of $ReS_2/ZnIn_2S_4$

Jiachao Xu [a], Wei Zhong [a], Feng Chen [a], Xuefei Wang [a,*,1], Huogen Yu [a,b,**,1]

[a] State Key Laboratory of Silicate Materials for Architectures and School of Chemistry, Chemical Engineering and Life Sciences, Wuhan University of Technology, Wuhan 430070, PR China

[b] Laboratory of Solar Fuel, Faculty of Materials Science and Chemistry, China University of Geosciences, Wuhan 430074, PR China

ARTICLE INFO

Keywords:
Photocatalysis
Hydrogen evolution
Cocatalyst
ReS_2
$ZnIn_2S_4$

ABSTRACT

Optimizing electron structure of H_2-evolution active sites to improve their catalytic efficiency is of great significance to develop efficient photocatalysts. Herein, an in situ cascade growth-induced strong coupling interface between ReS_2 and $ZnIn_2S_4$ nanolayers was developed to realize the electron structure optimization of S-active sites in ReS_2 cocatalyst, which can greatly improve the H_2-evolution efficiency of $ZnIn_2S_4$ photocatalyst. The in situ cascade growth of $ReS_2/ZnIn_2S_4$ includes initial formation of $ZnIn_2S_4$ nanolayers (ca. 200 °C) and their subsequent surface-induced production of ReS_2 (ca. 300–380 °C) in molten system. The resulting $ReS_2/ZnIn_2S_4$(3 wt%) shows a superior H_2-production rate, which is ca. 20.6 and 2.0 times higher than that of $ZnIn_2S_4$ and ReS_2-$ZnIn_2S_4$ (physical mixing), respectively. Besides the promoting transfer of photogenerated carriers, the cascade growth-induced strong coupling effect in the $ReS_2/ZnIn_2S_4$ can induce the construction of electron-deficient $S^{\delta+}$ site of ReS_2, causing the optimized binding strength of S-H bond and excellent H_2-evolution activity.

1. Introduction

Converting solar energy into hydrogen energy through photocatalytic technology is ideal route for solving non-renewable energy and environmental pollution [1–6]. However, the photocatalytic efficiency of monophase photocatalyst remains unsatisfactory, mainly due to the sluggish separation and migration kinetics of the photoinduced charge [7–11]. In order to promote the photoactivity of a single photocatalyst, numerous modification strategies, such as defect engineering, energy band regulation, and cocatalyst decoration, have been extensively investigated [12–14]. Among them, the loading of cocatalysts has been verified to be a promising approach, which not only trap electrons from semiconductors for the inhibition of charge recombination, but also offer sufficient active sites for accelerating catalytic reaction rate [15–18]. Compared to the typical noble metal (Pt, Pd, and Au) [19,20] and other conventional cocatalyst materials (Ni_2P, CoS_2, MoC, etc) [21–23], two-dimensional (2D) materials have attracted increasing interest in photocatalytic fields due to their many excellent characteristics, including that the special layered structure can greatly shorten the carrier transport distance and a larger specific surface area can provide numerous active sites for interfacial reactions [24–27]. Therefore, the integration of 2D cocatalysts can be expected to significantly boost the photoactivity of various photocatalysts and the development of 2D cocatalysts with excellent catalytic activity is highly desired.

In fact, the photoactivity of photocatalysts is also closely related to the interface contact type between the photocatalyst and cocatalyst [28,29]. Commonly, it is well accepted that the large contact area and intimate coupling at the interface of hybrid photocatalyst can effectively accelerate the migration rate of photo-excited carriers and thus boost photocatalytic activity [30]. Compared with 0D/0D, 0D/1D, 0D/2D and 1D/2D interfaces, the 2D/2D coupled interfaces have drawn wider attention in photocatalysis because both 2D components with wide lateral size and surface area can synchronously maximize the contact area, ensuring the sufficient charge transfer and trapping channels for the separation of photogenerated electron−hole pairs [31–33]. To date, numerous 2D/2D structures were synthesized to enhance the photocatalytic activity of photocatalysts. For instance, Pan's group reported the 2D Ti_2C-modified 2D g-C_3N_4 photocatalyst via hydrochloric acid

* Corresponding author.
** Corresponding author at: State Key Laboratory of Silicate Materials for Architectures and School of Chemistry, Chemical Engineering and Life Sciences, Wuhan University of Technology, Wuhan 430070, PR China.
E-mail addresses: xuefei@whut.edu.cn (X. Wang), huogenyu@163.com (H. Yu).
[1] Fax: 0086–27-87879468

https://doi.org/10.1016/j.apcatb.2023.122493
Received 17 November 2022; Received in revised form 1 January 2023; Accepted 19 February 2023
Available online 20 February 2023

etching (24 h) and subsequent high-temperature calcination (550 ℃, 4 h), which achieves the significantly enhanced photocatalytic H_2-generation activity [34]. Similarly, Zhu et al. prepared thin-layered black phosphorus through organic solvent-assisted ultrasonic stripping (N-Methylpyrrolidone, 4 h), which was further decorated on g-C_3N_4 photocatalyst surface by thermal polymerization process (550 ℃, 2 h) to markedly boost the H_2 evolution performance [35]. In addition, few-layer MoS_2 nanolayer-modified $CuInS_2$ was prepared by Yuan's group through two-step hydrothermal method (200 ℃, 24 h), which realizes the significantly enhanced photocatalytic H_2-production rate [36]. Based on the above results, it can be reasonably concluded that the construction of 2D/2D interface between cocatalyst and photocatalyst can greatly facilitate the efficient conversion of water into hydrogen. However, as discussed above, the main synthetic methods of 2D/2D hybrid photocatalyst usually involve complicated liquid phase exfoliation or high-press hydrothermal, and subsequent assembly process of ultrasonic or high-temperature calcination. Undeniably, the above multistep coupling process inevitably causes weak interaction between cocatalyst and photocatalyst, thus greatly impeding the charge transfer and suppressing the subsequent catalytic reaction [37–39]. To achieve a highly efficient photocatalytic system, the spatial integration between photocatalyst and cocatalyst to form the intimate contact interface is of great importance, which can distinctly improve the interfacial migration of photo-generated carriers [40,41]. Collectively, it is highly expected that if the above strong coupling effect between 2D cocatalyst and 2D semiconductor materials can be realized through a simple and efficient synthetic strategy, the H_2-evolution activity can further be enhanced in the fabricated 2D/2D hybrid photocatalyst.

In this work, we design and fabricate the 2D ReS_2-modified 2D $ZnIn_2S_4$ hetero-nanolayered photocatalyst (2D/2D $ReS_2/ZnIn_2S_4$) with strong coupling effect through an efficient and convenient molten salt method. Herein, with gradually increasing synthetic temperature in molten KSCN system, the 2D $ZnIn_2S_4$ nanolayers are preferentially produced at low temperature (ca. 200 °C), which can further act as a support to induce the in-situ nucleation and growth of 2D ReS_2 nanolayer at a higher temperature (ca. 300–380 °C), causing the final formation of strong-coupled 2D/2D $ReS_2/ZnIn_2S_4$ photocatalyst. The photocatalytic performance test demonstrates that the $ReS_2/ZnIn_2S_4$(3 wt%) photocatalyst exhibits a maximum H_2-production activity, which is nearly 20.6 and 2.0-fold higher than that of the pristine $ZnIn_2S_4$ and ReS_2-$ZnIn_2S_4$ samples (prepared by physical mixing), respectively. The enhanced photocatalytic performance is accounted by the strong coupling interface of $ReS_2/ZnIn_2S_4$, which not only effectively promotes the directional transfer of photo-excited electrons from $ZnIn_2S_4$ to ReS_2 cocatalyst, but also efficaciously induces the formation of electron-deficient $S^{\delta+}$ site of ReS_2, thus greatly enhancing the overall H_2-evolution rate. This work presents a facile strategy for the preparation of 2D/2D hetero-photocatalyst and provides deep insights to regulate material interfaces for efficient solar H_2-evolution.

2. Experimental section

2.1. Synthesis of 2D/2D $ReS_2/ZnIn_2S_4$

The strong-coupled 2D/2D $ReS_2/ZnIn_2S_4$ photocatalyst was prepared by a molten salt method. Typically, the potassium thiocyanate (KSCN) was served as both molten salt and sulfur source, while zinc acetate dihydrate ($Zn(CH_3COOH)_2{\cdot}2\ H_2O$, 104 mg), anhydrous indium trichloride ($InCl_3$, 209 mg), and sodium perrhenate ($NaReO_4$, 6.4 mg) were used as the transition metal precursors. First, excessive amounts of KSCN (10 g) were mixed with the above transition metal precursors, and then the mixture was transferred into the quartz and was heated to 380 °C at a rate of 3 °C/min and held for 2 h under an air atmosphere. After that, the product was cooled to room temperature and washed with deionized water to eliminate soluble salts. Finally, the insoluble product was collected via filtration and dried at 70 ℃ to obtain the strong-coupled 2D/2D $ReS_2/ZnIn_2S_4$ photocatalyst.

To explore the influence of 2D ReS_2 nanolayer on the H_2-production rate of $ZnIn_2S_4$, the theoretical mass ratio of ReS_2 to $ZnIn_2S_4$ was adjusted as 0.5, 1, 3, and 5 wt%, and the obtained photocatalysts were marked as $ReS_2/ZnIn_2S_4$ (X wt%), where x represented the amount of 2D ReS_2 nanolayer.

Synthesis of ReS_2 nanolayer: Pristine 2D ReS_2 nanolayer was also synthesized via the same route as $ReS_2/ZnIn_2S_4$ by only using $NaReO_4$ as the precursor.

Synthesis of pristine $ZnIn_2S_4$: Pristine 2D $ZnIn_2S_4$ nanolayer was also synthesized via the same route as $ReS_2/ZnIn_2S_4$ by only using zinc acetate dihydrate and anhydrous indium trichloride as the precursors.

Synthesis of physically mixed ReS_2-$ZnIn_2S_4$: As a comparison, the physically mixed ReS_2-$ZnIn_2S_4$ sample was fabricated via the traditional mixing method. Briefly, 5 mg of 2D ReS_2 nanolayer was dispersed into 10 mL of ethanol solution and sonicated for 2 h to obtain a homogeneous dispersion. Then, 80 mg of the as-prepared $ZnIn_2S_4$ is ultrasonically dispersed into 50 mL of water, followed by the addition of 4.8 mL ReS_2-ethanol dispersion drop by drop under stirring. After stirring at 70 ℃ for two hours, the product was collected by centrifugation and dried in oven to harvest ReS_2-$ZnIn_2S_4$(3 wt%) sample.

2.2. Characterization

The crystal information of the photocatalysts was obtained by XRD (Cu Kα radiation, Rigaku). To disclose the morphology and microstructure of the synthesized photocatalysts, the scanning electron microscope (SEM; JSM-7500 F) and transmission electron microscopy (TEM; JEM-2100 F) were applied to study the morphology of photocatalyst. A UV-2450 spectrophotometer was utilized to acquire UV–vis spectra. Contact potential difference (CPD) was measured on a kelvin probe apparatus (Instytut Fotonowy, Poland). An ESCALAB 10 electron spectrometer was used to collect in situ X-ray photoelectron spectroscopy (XPS) spectra. Ex-situ XPS profiles were gathered on a KRATOA XSAM800 system. Photoluminescence spectra (PL) were obtained by Edinburgh LP 980 spectrophotometer. The time-resolved photoluminescence (TRPL) spectra were acquired using an FLS1000 fluorescence lifetime spectrophotometer (Edinburgh, Instruments, UK). In-situ X-ray photoelectron spectroscopic spectra were obtained from an electron spectrometer (ESCALAB 210, VG, UK).

2.3. Photocatalytic activity tests

The 50 mg as-synthesized photocatalyst was dispersed in an aqueous solution (80 mL) containing lactic acid (10 vol%) as a sacrificial electron donor. Then, the reactant solution was degassed with pure N_2 for 20 min to remove air prior, and subsequently irradiated by four 3-W 420 nm LED lamps. Herein, the amount of produced H_2 was analyzed by Shimadzu gas chromatography (GC-2014 C, Japan).

3. Results and discussion

3.1. The in situ cascade growth of $ReS_2/ZnIn_2S_4$ photocatalyst

In this study, an interfacial S-induced in situ cascade growth was utilized to achieve the orderly growth of ReS_2 on $ZnIn_2S_4$ surface to form a strong-coupled 2D/2D $ReS_2/ZnIn_2S_4$ hybrid photocatalyst in a molten salt system, as illustrated in Fig. 1. Typically, a series of $Zn(CH_3COOH)_2$, $InCl_3$, and $NaReO_4$ metal salt is thoroughly mixed with excessive KSCN power to obtain a mixture percussor in a quartz crucible. Herein, the KSCN as a molten salt can not only serve as S source for ReS_2 and $ZnIn_2S_4$, but also provide an ideal fluid environment to synthesize strong-coupled 2D/2D $ReS_2/ZnIn_2S_4$ photocatalyst during the following molten salt process (Fig. S1 and S2) [42,43]. With increasing calcination temperature to ca. 170 °C, the KSCN is first self-ionized to produce a uniform and fluid molten salt system with massive SCN^- ions, which can

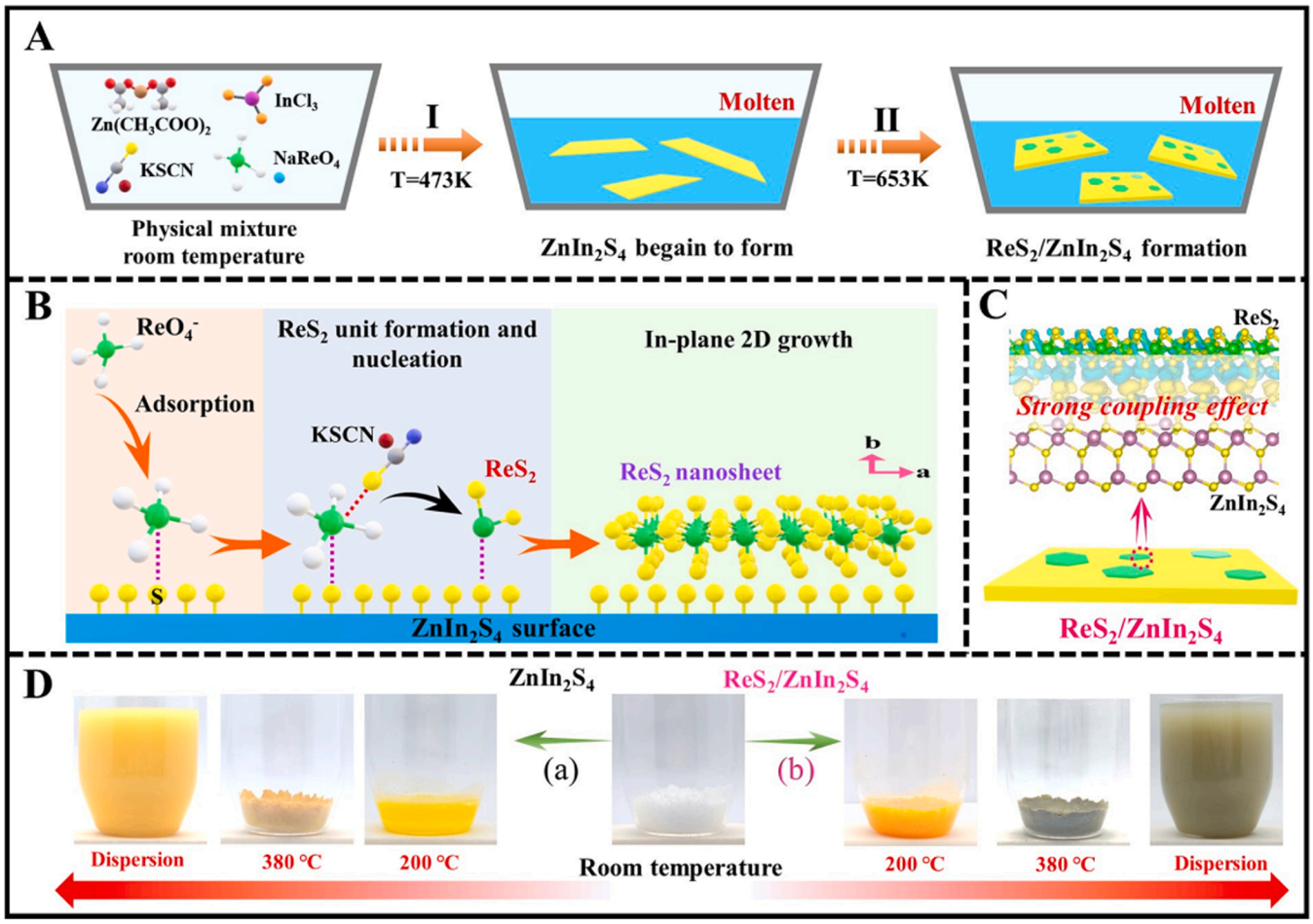

Fig. 1. (A) Schematic diagram illustrating the in-situ cascade growth of $ReS_2/ZnIn_2S_4$. (B) Detailed cascade growth mechanism of ReS_2 on $ZnIn_2S_4$ surface. (C) The model structure of $ReS_2/ZnIn_2S_4$ with strong coupling effect. (D) The corresponding photographs for pure $ZnIn_2S_4$ and $ReS_2/ZnIn_2S_4$.

tightly combine with Zn^{2+} and In^{3+} to form corresponding $[Zn(SCN)_4]^{2-}$ and $[In(SCN)_6]^{3-}$ complexes in the molten system (Eq. (2)) [44]. As the reaction temperature increases to 200–250 °C, the as-formed $[Zn(SCN)_4]^{2-}$ and $[In(SCN)_6]^{3-}$ complexes can occur self-decomposition reaction to produce thin-layered $ZnIn_2S_4$ nanolayers (Eq. (3)) (Fig. 1A-I), which can be clearly demonstrated by the color change from colorlessness to bright yellow in Fig. 1D-(a). Considering the typical layered structure of $ZnIn_2S_4$ nanolayers with massive surface S atoms (Fig. S3), the ReO_4^- ions in the KSCN molten salt system are preferably and tightly adsorbed on the surface S atom sites of $ZnIn_2S_4$ nanolayers, which offers an outstanding platform for the following growth of ReS_2 nanolayers (Fig. 1A-II). With further increasing calcination temperature to ca. 300–380 °C, the adsorbed ReO_4^- ions on the $ZnIn_2S_4$ surface can in-situ react with the free SCN^- ions to quickly form ReS_2 seeds (Eq. (4)) (Fig. 1B and Fig. S4). Benefiting from the interface-induced effect of the layered $ZnIn_2S_4$ nanolayers, the fabricated ReS_2 seeds can further in-plane grow to form the final ReS_2 nanolayers (as illustrated in Fig. 1D-(b)), causing a strong-coupled interface between the layered $ZnIn_2S_4$ nanolayers and ReS_2 nanolayers in the 2D/2D $ReS_2/ZnIn_2S_4$ photocatalyst (Fig. 1C and Fig. S5). To verify the proposed interfacial S-induced in-situ growth mechanism, for comparison, the blank CdS and ReS_2/CdS samples are also fabricated with the similar strategy as $ReS_2/ZnIn_2S_4$ (Fig. S6). Different from surface S atomic layer of $ZnIn_2S_4$, the exposed atoms on the CdS surface are usually Cd and S elements [45]. Obviously, it can be observed that the as-synthesized ReS_2 nanolayers possess an agglomerated nanoflower-like morphology and randomly load on the hexagonal CdS surface (Fig. S7), which can be ascribed to the absence of interface-induced effect of the hexagonal CdS surface to supply the planar 2D growth for ReS_2 nanolayers. Therefore, it can be concluded that the interfacial S-induced in situ cascade growth facilitates the in-plane growth of 2D ReS_2 nanolayer onto layered $ZnIn_2S_4$ nanolayers, thereby forming a strong-coupled interface in 2D/2D $ReS_2/ZnIn_2S_4$ hybrid photocatalyst.

$$KSCN \leftrightharpoons K+ + SCN- \quad (1)$$

$$10SCN^- + Zn^{2+} + In^{3+} \rightarrow [Zn(SCN)_4]^{2-} + [In(SCN)_6]^{3-} \quad (2)$$

$$[Zn(SCN)_4]^{2-} + 2[In(SCN)_6]^{3-} \rightarrow ZnIn_2S_4 + 8CN^- + 3(SCN)_2 \quad (3)$$

$$ReO_4^- + SCN^- \rightarrow ReS_2 + OCN^- \quad (4)$$

3.2. *The characterization of cascade growth-induced strong coupling $ReS_2/ZnIn_2S_4$ photocatalysts*

The morphology and microstructure of the obtained strong-coupled 2D/2D $ReS_2/ZnIn_2S_4$ hetero-nanolayers were firstly disclosed by transmission electron microscopy (TEM). As shown in Fig. 2A and B, the ReS_2 exhibits a typical 2D nanolayer structure with a size of ca. 20 nm, and is uniformly anchored on the ultrathin lamellar $ZnIn_2S_4$ surface to form the ultimate 2D/2D hetero-nanolayered property. The select area electron diffraction (SAED) (inset of Fig. 2C) of ReS_2 nanolayer shows the uniform arrangement of diffraction patterns, proving their single-crystal nature. Meanwhile, a more detailed observation on the 2D ReS_2 nanolayer (Fig. 2D) corroborates that the ReS_2 nanolayers present orientational growth on $ZnIn_2S_4$ surface, which is mainly attributed to the

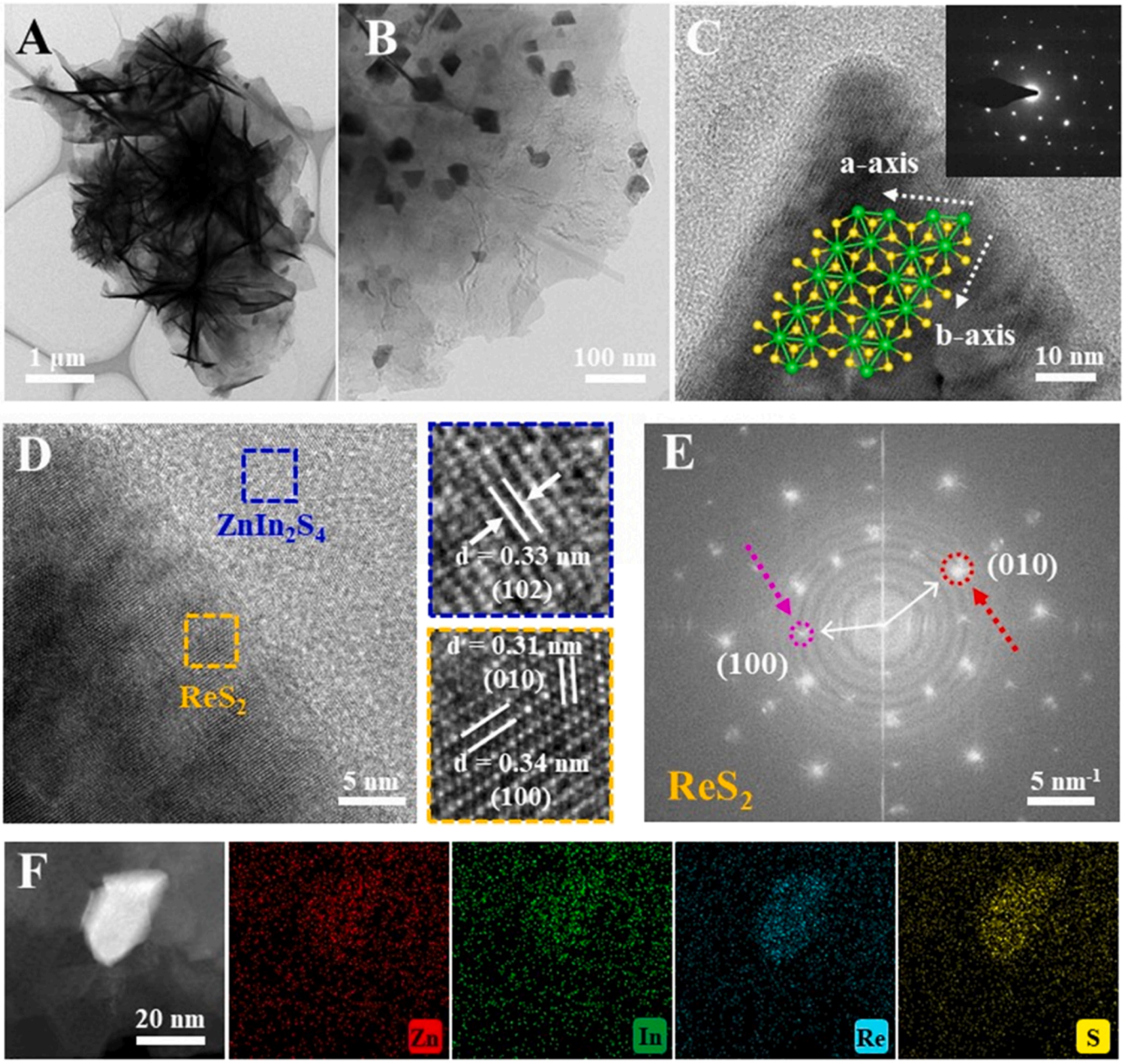

Fig. 2. (A-D) TEM/HRTEM images of $ReS_2/ZnIn_2S_4$ photocatalyst via in-situ cascade growth. (E) Fast Fourier transform (FFT) image of ReS_2. (F) HAADF-STEM and element mapping images.

interfacial S-induced effect as discussed in Fig. 1. Furthermore, the high-resolution TEM images of the 2D/2D $ReS_2/ZnIn_2S_4$ photocatalysts disclose that two characteristic lattice spacings of 0.34 and 0.31 nm could be ascribed to the (100) and (010) planes of 2D ReS_2 nanolayers, respectively [46], and the lattice spacing of 0.33 nm can also be indexed to the (102) plane of $ZnIn_2S_4$ nanolayers. In this case, the FFT images in Fig. 2E further reveal that the ReS_2 nanolayer presents two major (100) and (010) planes, highlighting its preferential [001] orientation growth in the 2D/2D $ReS_2/ZnIn_2S_4$ photocatalysts [47]. Thus, owing to the interfacial S-induced effect, the ReS_2 can preferentially grow on the surface of layered $ZnIn_2S_4$ to form anisotropic 2D crystal shapes, which is beneficial to fabricating intimate contact interface in 2D/2D $ReS_2/ZnIn_2S_4$ hetero-nanolayer photocatalysts. Additionally, for the 2D/2D $ReS_2/ZnIn_2S_4$ photocatalysts, the signal peaks of Zn, In, Re, and S elements can be observed in EDX spectrum (Fig. S8) and the corresponding elemental mappings further display the same dispersion of Re and S elements (Fig. 2F), fiercely re-evidencing the successful anchor of ReS_2 nanolayer on lamellar $ZnIn_2S_4$ surface. The ICP-OES characterization demonstrates that the amount of Re elements is about 2.74 wt% and the atomic ratio of Zn to In is 1:2 in the 2D/2D $ReS_2/ZnIn_2S_4$, which further manifests the effective integration of ReS_2 and $ZnIn_2S_4$ via the innovative molten salt method. Obviously, the interfacial S-induced orientation growth of ReS_2 nanolayer on the $ZnIn_2S_4$ surface promotes the formation of strong-coupled 2D/2D $ReS_2/ZnIn_2S_4$ photocatalyst.

The constructed strong-coupled interface between ReS_2 and $ZnIn_2S_4$ nanolayers can further be determined by XRD, Raman spectra, XPS, and UV–vis spectroscopy. As displayed in Fig. 3A, the XRD patterns of $ZnIn_2S_4$ and $ReS_2/ZnIn_2S_4$ composites present analogous diffraction peaks of hexagonal $ZnIn_2S_4$, while the typical ReS_2 peaks (Fig. S9) cannot be identified in the 2D/2D $ReS_2/ZnIn_2S_4$ photocatalyst due to its relatively low content [48]. However, the characteristic Raman peaks at 151.5 cm^{-1} and 243.7 cm^{-1} are observed (Fig. 3B), which can be

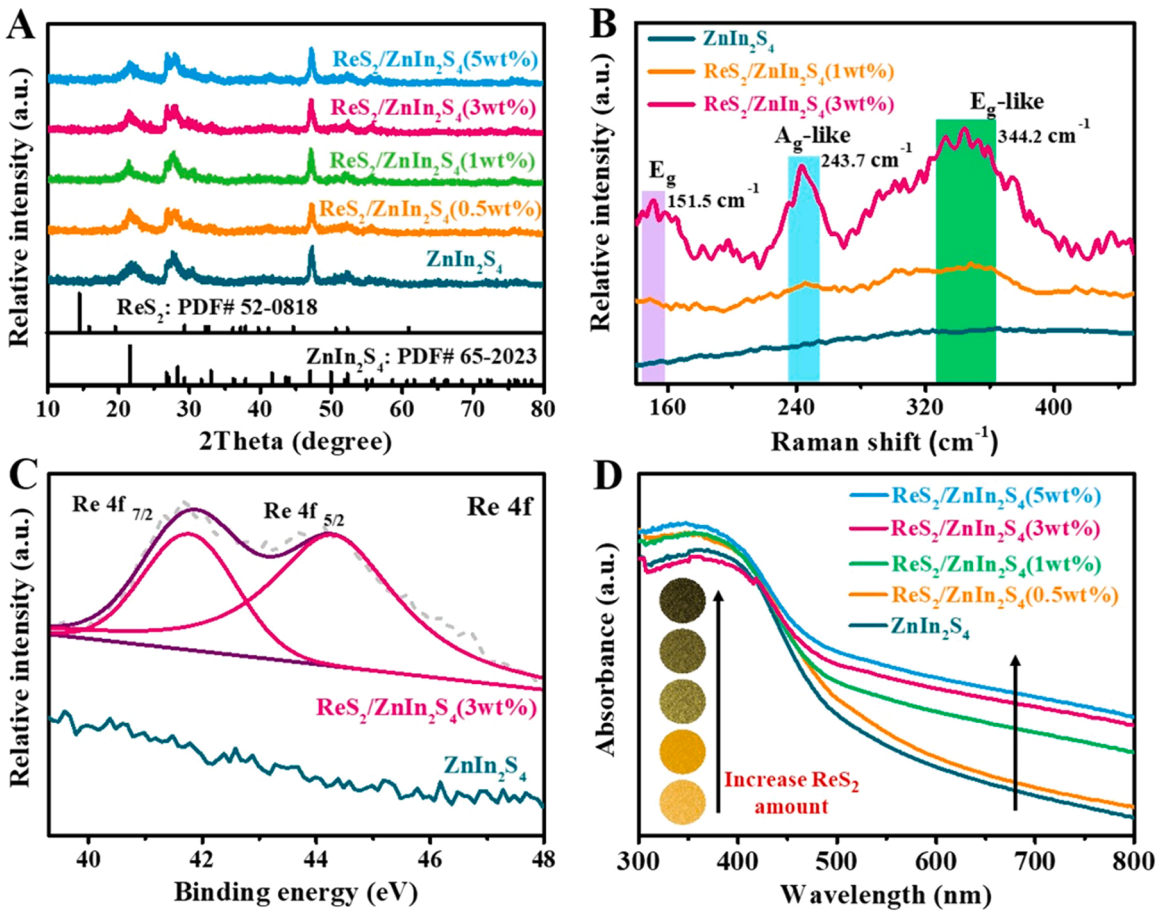

Fig. 3. (A) XRD, (B) Raman spectra, (C) high-resolution XPS spectra of Re 4f and (D) UV–vis spectra of $ZnIn_2S_4$ and $ReS_2/ZnIn_2S_4$ samples with different mass of ReS_2.

ascribed to the E_g- and A_g-like models of ReS_2 in the 2D/2D $ReS_2/ZnIn_2S_4$ photocatalyst [49], fiercely confirming the formation of ReS_2 on the $ZnIn_2S_4$ surface. More importantly, compared with bare ReS_2 (Fig. S10), the E_g- and A_g-like bands of 2D/2D $ReS_2/ZnIn_2S_4$ reveal a red shift, which can be ascribed to the strong interface coupling between ReS_2 and $ZnIn_2S_4$ nanolayers. In addition, XPS characterization was employed to further testify the formation of 2D/2D $ReS_2/ZnIn_2S_4$ hybrid (Fig. 3C). Typically, two dominant peaks of Re $4f_{7/2}$ and Re $4f_{5/2}$ core-level peaks are located at ~41.5 and ~44.2 eV in $ReS_2/ZnIn_2S_4$ sample [50], respectively, indicating the successful integration of ReS_2 nanolayer on $ZnIn_2S_4$ surface. In this case, the light-adsorption property of the 2D/2D $ReS_2/ZnIn_2S_4$ photocatalyst was scrutinized by diffuse reflectance UV–vis spectroscopy, as performed in Fig. 3D. Obviously, the absorption edge of pure $ZnIn_2S_4$ around 518 nm can be identified, which agrees well with the band gap value of about 2.39 eV. After the integration with ReS_2, the resultant 2D/2D $ReS_2/ZnIn_2S_4$ photocatalysts clearly present a broader visible-light response (450–800 nm). In addition, with increasing the amount of ReS_2 nanolayer, the visible-light absorbance can be further strengthened. Meanwhile, the color of various samples presents a gradually deepening trend with increasing ReS_2 loading amount, manifesting the successful and controllable preparation of 2D/2D $ReS_2/ZnIn_2S_4$ hetero-layered photocatalysts via the effective and convenient molten salt method.

3.3. Photocatalytic performance and mechanism

The photocatalytic activities of in situ cascade growth-induced strong coupled $ReS_2/ZnIn_2S_4$ photocatalysts were tested under visible light using lactic acid as a sacrificial reagent. In this case, the photocatalyst dosage of 50 mg were applied in our experiments to ensure their typicality, feasibility and effectiveness (Fig. S11). As observed in Fig. 4A and B, it can be found that pure $ZnIn_2S_4$ exhibits the lowest H_2-evolution rate due to the rapid recombination of photo-induced carriers and the lack of catalytic active sites [51,52]. However, after loading 2D ReS_2 nanolayer, the photocatalytic performance of 2D/2D $ReS_2/ZnIn_2S_4$ with strong-coupled interface is greatly improved. Especially, the H_2-evolution rate of the 2D/2D $ReS_2/ZnIn_2S_4$(3 wt%) reaches an optimum value as high as 2240 μmol g^{-1} h^{-1}, which is approximately 20.61-fold higher than that of pure $ZnIn_2S_4$ nanolayers (a H_2-evolution rate of 103 μmol g^{-1} h^{-1}). Notably, the photocatalytic performance of the obtained 2D/2D $ReS_2/ZnIn_2S_4$(3 wt%) is obviously superior than that of the physical mixing ReS_2-$ZnIn_2S_4$(3 wt%) sample (1105 μmol g^{-1} h^{-1}), which can be attributed to its strong coupling interface via the unique interfacial S-induced synthesis strategy. It should also be mentioned that the boosted photoactivity of 2D/2D $ReS_2/ZnIn_2S_4$(3 wt%) samples is superior to most reported $ZnIn_2S_4$-based photocatalysts under visible light (Table S2). Moreover, after five cycles with a total irradiation time of 25 h, the 2D/2D $ReS_2/ZnIn_2S_4$(3 wt%) photocatalyst still remains a steady H_2-evolution activity (Fig. 4C). After photocatalytic H_2 evolution, the morphology and crystal structure of the resulting 2D/2D $ReS_2/ZnIn_2S_4$ nanolayers are well maintained (Figs. S12 and 13), displaying its good photostability (with the TON of 569.42). To further verify the above H_2-evolution activity from the photo-absorption of $ZnIn_2S_4$ semiconductor, the wavelength-dependent apparent quantum efficiency (AQE) of $ReS_2/ZnIn_2S_4$(3 wt%) was measured, as illustrated in Fig. 4D. It is clear that the change of AQE value over the 2D/2D $ReS_2/ZnIn_2S_4$(3 wt%) photocatalyst keeps the same trend as the

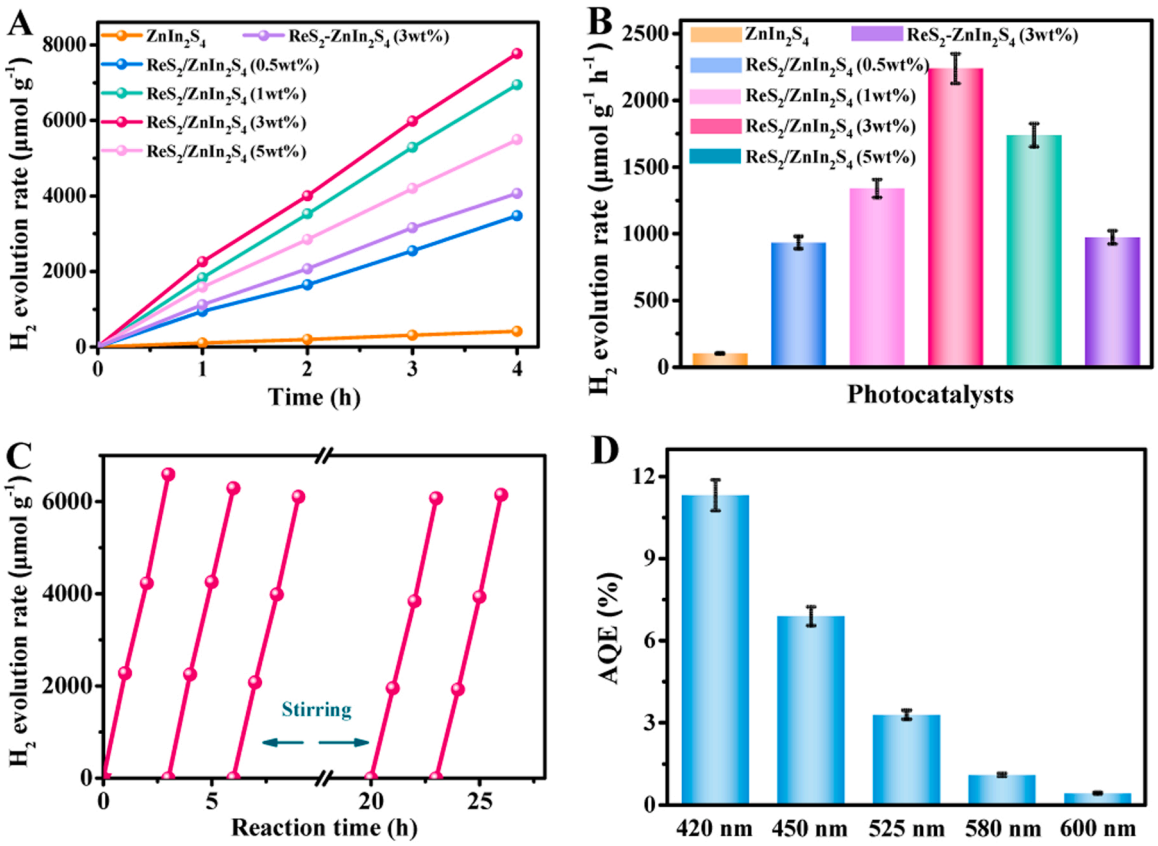

Fig. 4. (A) H_2 evolution amount at different irradiation time and (B) H_2-evolution rate of $ZnIn_2S_4$ and $ReS_2/ZnIn_2S_4$ photocatalysts. (C) Cycling stability test and (D) wavelength-dependent apparent quantum yield (AQY) of $ReS_2/ZnIn_2S_4$(3 wt%).

absorption spectrum of $ZnIn_2S_4$. Therefore, the strong-coupled $ReS_2/ZnIn_2S_4$ photocatalyst prepared by in-situ cascade growth possesses outstanding photocatalytic H_2-generation activity and stability.

Based on the above photocatalytic results, the hetero-layered 2D/2D $ReS_2/ZnIn_2S_4$ photocatalyst exhibits a superior H_2-evolution activity, which is mainly caused by in-situ cascade growth induced strong coupling effect between ReS_2 and $ZnIn_2S_4$ nanolayers, as demonstrated in XPS characterization and density functional theory (DFT) calculation. As displayed in Fig. 5A, compared to blank $ZnIn_2S_4$ and physically mixed ReS_2-$ZnIn_2S_4$ samples, it is found that the dominant peaks of Zn 2p at 1022.4 and 1045.5 eV present a remarkably negative shift for the 2D/2D $ReS_2/ZnIn_2S_4$ photocatalyst, manifesting the migration of free electrons from 2D ReS_2 to $ZnIn_2S_4$ nanolayers due to the in-situ cascade growth induced strong coupling effect. The above results can be further confirmed by the same shift of binding energy for In 3d in Fig. S14. On the contrary, the binding energy of Re 4f moves towards positive values compared with the ReS_2-$ZnIn_2S_4$ sample (Fig. 5B), evidently demonstrating the formation of a strong-coupled interface in the 2D/2D $ReS_2/ZnIn_2S_4$ photocatalys [53]. To better testify the strong coupling effect in the 2D/2D $ReS_2/ZnIn_2S_4$ hetero-nanolayer, DFT calculation is further performed. The density of state (DOS) was first conducted and shown in Fig. 5C. Noticeably, the electronic states of Re atoms are overlapped with those of the Zn, In, and S atoms in the 2D/2D $ReS_2/ZnIn_2S_4$ sample, which can be attributed to the strong coupling effect between ReS_2 and $ZnIn_2S_4$ [54]. The above strong coupling effect in 2D/2D $ReS_2/ZnIn_2S_4$ can also be directly revealed by the simulated charge distribution and the plots of planar-averaged charge density difference (Fig. 5D). Obviously, the charge redistribution is mainly focused on their contact interface layer and the free electrons on the ReS_2 are directly transferred to the $ZnIn_2S_4$ via their strong-coupled interface. As is known to all, the rate of interfacial catalytic reaction is closely related to the electronic structure of active sites. In this case, it is expected that the electron migration caused by strong coupling effect in 2D/2D $ReS_2/ZnIn_2S_4$ can greatly improve the catalytic efficiency of interficial S site in ReS_2. Herein, Bader charge analysis (Fig. 5E) is performed to further disclose the change of electron density on S-site in ReS_2 cocatalyst. Evidently, compared to blank ReS_2, the electron density of S site in the 2D/2D $ReS_2/ZnIn_2S_4$ hybrid is significantly reduced (from +0.56 to +0.43 e^-) and thus forming the electron-deficient S site ($S^{\delta+}$) on the surface of ReS_2 nanolayer, which can effectively enhance the adsorption strength of H* to promote H_2-generation activity (Fig. 5F). Subsequently, the adsorption Gibbs free energy of intermediate state H* (ΔG_{H^*}) was calculated and performed in Fig. 5G [55,56]. It can be seen that the ΔG_{H^*} of surface S sites in ReS_2-$ZnIn_2S_4$ is 1.76 eV and indicates the weak binding of H* with S sites (Fig. 5G). After forming the 2D/2D $ReS_2/ZnIn_2S_4$ composite, the corresponding ΔG_{H^*} value is optimized to 1.44 eV, which is more satisfied with the theoretical optimum (ΔG_{H^*} = 0 eV), manifesting an enhanced H* adsorption capacity of the S site for the following promoted H_2 formation (Fig. S15). Therefore, all the theoretical and experimental results above illustrate the promotion influence of the in situ cascade growth-induced strong coupling effect in 2D/2D $ReS_2/ZnIn_2S_4$ photocatalyst on the generation of electron-deficient $S^{\delta+}$ site and thus increased catalytic-efficiency of the S sites.

To further explore the promotional effect of strong coupling effect induced by in situ cascade growth on photogenerated carrier transfer for 2D/2D $ReS_2/ZnIn_2S_4$, the Kelvin probe test and in situ irradiated XPS characterization were performed (Fig. 6). First, according to the obtained potential difference (CPD) data from the Kelvin probe test, the work function of $ZnIn_2S_4$ is calculated to be 4.37 eV and that of ReS_2 is 4.23 eV (Fig. 6A). Moreover, the performed DFT calculations theoretically prove that the work function of $ZnIn_2S_4$ is higher than that of ReS_2 (Fig. S16). As a result, when the 2D ReS_2 was in-situ grown onto the 2D $ZnIn_2S_4$ to produce the 2D/2D $ReS_2/ZnIn_2S_4$ hybrid with a strong-

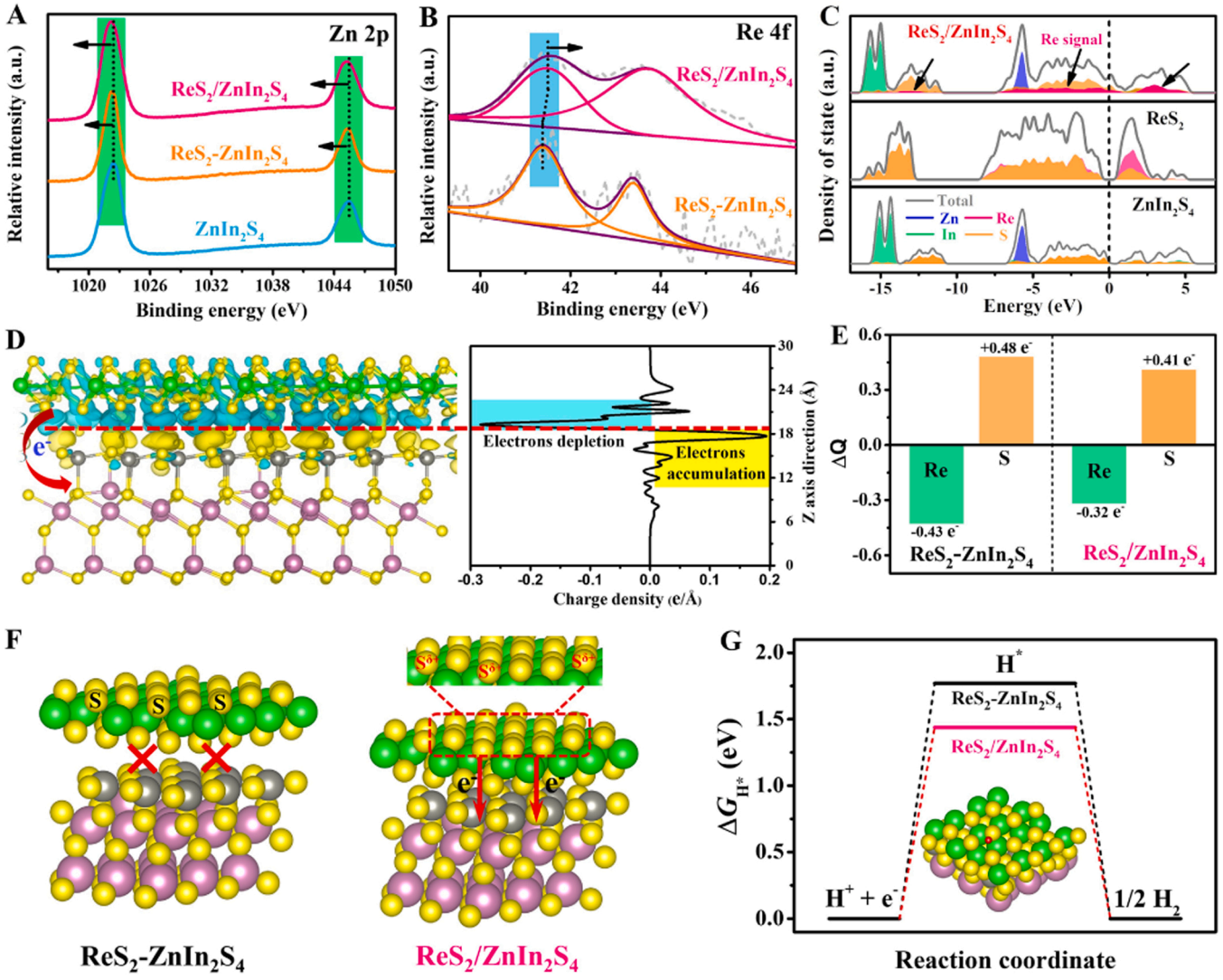

Fig. 5. (A, B) High-resolution XPS spectra of Zn 2p and Re 4f for $ZnIn_2S_4$, ReS_2-$ZnIn_2S_4$ and ReS_2/$ZnIn_2S_4$ and (C) their corresponding calculated density of state. (D) Simulated charge distributions at the interface of ReS_2/$ZnIn_2S_4$ and its corresponding planar averaged charge-density difference, where the blue and yellow region represents the consumption and accumulation of electrons, respectively. (E) Bader charge analysis, (F) the schematic diagram of improving active site efficiency by strong coupled interface and (G) H_2 absorption free energies for ReS_2-$ZnIn_2S_4$ and ReS_2/$ZnIn_2S_4$.

coupled interface, the free electrons would migrate from ReS_2 to $ZnIn_2S_4$ nanolayer through their strong-coupled interface, causing the production of a built-in electric field pointed from $ZnIn_2S_4$ to ReS_2 (Fig. 6E-I) [57,58]. It can be seen from the in-situ XPS data that compared to dark conditions, the binding energy of Zn 2p and In 3d moved to a more positive position (Fig. 6B and C) while the Re 4f shifted to a more negative position (Fig. 6D) in light irradiation, suggesting that the photogenerated electrons on 2D $ZnIn_2S_4$ can effectively transfer to ReS_2 nanolayer. The above electron migration behavior is greatly driven by the created internal electric field from ReS_2 to $ZnIn_2S_4$, which effectively inhibits the charge recombination to provide massive photo-excited electrons for subsequent catalytic H_2-evolution reactions (Fig. 6E-II).

Based on the above results, an underlying mechanism is proposed for the largely enhanced photocatalytic activity of in situ cascade growth-induced strong coupled ReS_2/$ZnIn_2S_4$ photocatalysts, as shown in Fig. 7. Herein, owing to the interfacial S-induced in situ cascade growth, the 2D ReS_2 nanolayers are evenly anchored on the lamellar $ZnIn_2S_4$ surface to induce the strong coupling effect, thus endowing the resulting 2D/2D ReS_2/$ZnIn_2S_4$ hybrid with sufficient contact area and electron transfer channels. In addition, a built-in electric field from ReS_2 to $ZnIn_2S_4$ can be created due to the difference in work function, thus facilitating the subsequent transfer of photoinduced electrons from $ZnIn_2S_4$ to ReS_2. Under visible-light irradiation, the electrons in the valence band of $ZnIn_2S_4$ are excited to its conduction band, leaving the positively charged holes in the VB. Afterward, the excited electrons can be further transferred to surface-grown ReS_2 nanolayer through the strong-coupled interface in the 2D/2D ReS_2/$ZnIn_2S_4$ photocatalysts, largely suppressing the recombination of charge carriers. It is worth noting that the strong coupling effect in the 2D/2D ReS_2/$ZnIn_2S_4$ photocatalyst can not only facilitate the migration of photoinduced electrons, but also simultaneously reduce the electron density of the active S site to produce electron-deficient S site on ReS_2 nanolayers. Therefore, when photoexcited electrons transfer to ReS_2 cocatalyst, the as-formed electron-deficient S site would efficiently combine with H* and greatly enhance the photocatalytic H_2-evolution performance.

To further examine the above proposed photocatalytic mechanism, a series of photoluminescence (PL), photo- and electrochemical characterizations were carried out. As shown in Fig. S17A, the steady-state PL spectra of the 2D/2D ReS_2/$ZnIn_2S_4$ photocatalysts show obvious quenching than pure $ZnIn_2S_4$ and ReS_2-$ZnIn_2S_4$, indicating the efficient charge separation and transfer of photogenerated charges between ReS_2 and $ZnIn_2S_4$. Besides, compared with pristine $ZnIn_2S_4$ (τ_{ave} = 4.55 ns)

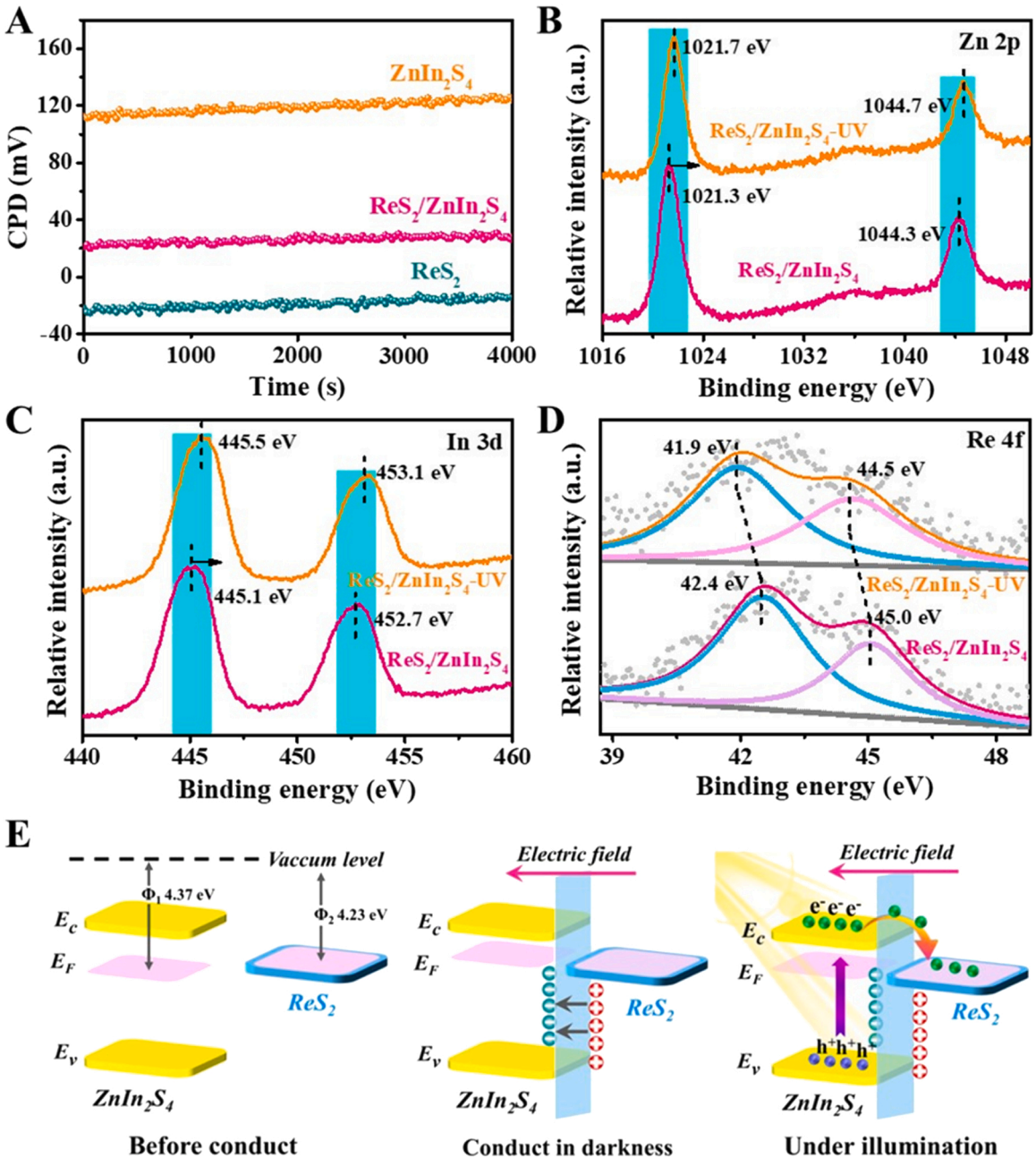

Fig. 6. (A) Contact potential difference of the $ZnIn_2S_4$, ReS_2, and $ReS_2/ZnIn_2S_4$ samples. In-situ XPS spectra of (B) Zn 2p, (C) In 3d, and (D) Re 4f for $ReS_2/ZnIn_2S_4$ sample before and after visible-light irradiation. (E) The schematic diagram of photogenerated electron transfer before and after light irradiation.

and ReS_2-$ZnIn_2S_4$ (τ_{ave} = 6.14 ns), the accelerated decay of time-resolved photoluminescence (TRPL) and significant prolongation of charge-carrier averaged lifetimes (τ_{ave} = 11.07 ns) for the 2D/2D ReS_2/$ZnIn_2S_4$ photocatalysts manifest an effectively improved carrier separation due to the strong-coupled interface (Fig. S17B) [59]. Moreover, the 2D/2D $ReS_2/ZnIn_2S_4$ hybrid possesses a smaller EIS radius and stronger photocurrent density than the bare $ZnIn_2S_4$ and ReS_2-$ZnIn_2S_4$, reconfirming the fastest interfacial charge migration in the 2D/2D $ReS_2/ZnIn_2S_4$ sample (Fig. S17C and D). Generally, the photocatalytic H_2-evolution reaction thermodynamically depends on the conductor band (CB) potential. As revealed by the Mott-Schottky plots (Fig. S18), the $ReS_2/ZnIn_2S_4$ photocatalyst exhibits n-type semiconductor and the CB value is calculated to be − 0.58 V (vs. NHE), manifesting the superior capacity for the reduction of H^+ to H_2. The linear sweep voltammetry results (Fig. S19) show that the 2D/2D $ReS_2/ZnIn_2S_4$ photocatalyst possesses a larger cathode current than the $ZnIn_2S_4$ and ReS_2-$ZnIn_2S_4$, further suggesting the efficient interfacial H_2-production due to the elevated catalytic-efficiency of active S sites on 2D ReS_2 nanolayer. Collectively, the systematic photoluminescence, photo- and electrochemical properties clearly demonstrate the efficient separation of electron-hole pair and high surface reaction rate for the 2D/2D $ReS_2/ZnIn_2S_4$ hetero-layered photocatalyst, which can be attributed to the strong-coupled interface between ReS_2 and $ZnIn_2S_4$ component.

4. Conclusions

To summarize, an in situ cascade growth-induced strong coupled $ReS_2/ZnIn_2S_4$ photocatalyst was successfully constructed in KSCN molten salt system. It is found that the ReS_2 nanolayers are orientationally grown on lamellar $ZnIn_2S_4$ surface via an interfacial S-induced

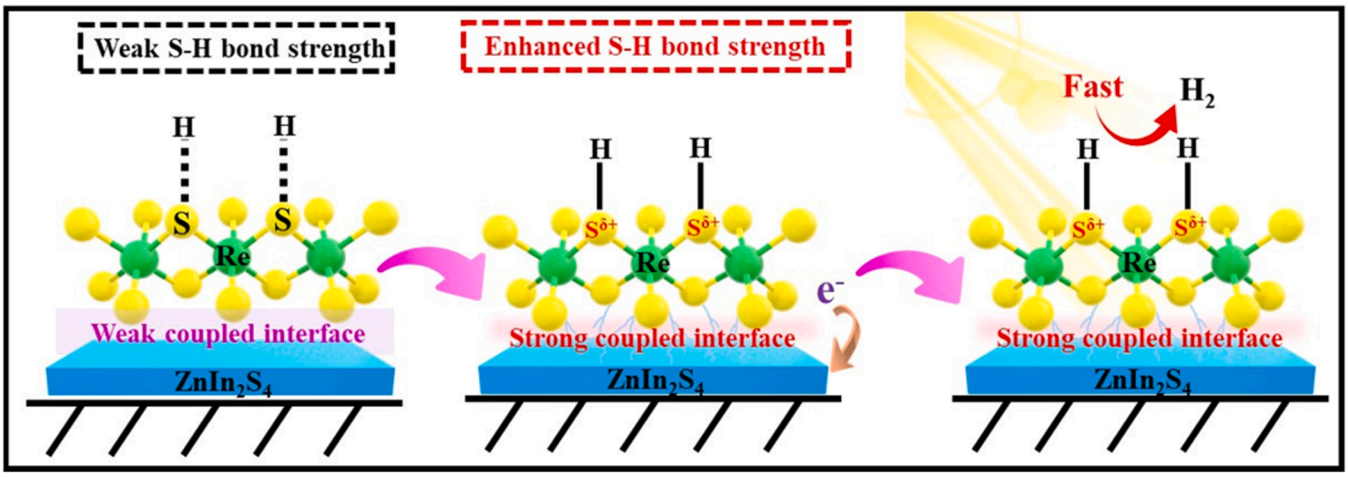

Fig. 7. Proposed photocatalytic H_2-generation mechanism of cascade growth-induced strong coupled $ReS_2/ZnIn_2S_4$ photocatalyst.

in situ cascade growth, leading to the formation of a strong-coupled interface in the 2D/2D $ReS_2/ZnIn_2S_4$ photocatalysts. Photocatalytic tests demonstrated that the fabricated strong-coupled 2D/2D $ReS_2/ZnIn_2S_4$(3 wt%) photocatalyst achieved a high-efficiency photocatalytic hydrogen production rate of 2240 μmol g^{-1} h^{-1} with an AQE of 11.32% (420 nm). Combining experimental characterizations and theoretical calculations, the outstanding photocatalytic performance of 2D/2D $ReS_2/ZnIn_2S_4$ photocatalyst can be attributed to the strong coupling effect between ReS_2 and $ZnIn_2S_4$ nanolayer via in situ cascade growth. Specifically, the strong coupling effect can decrease the charge transfer barrier to accelerate photoinduced charge separation, and more importantly, effectively induces the formation of electron-deficient $S^{\delta+}$ site of ReS_2 to boost their catalytic H_2-evolution efficiency. This work emphasizes the rational design of the coupling interfaces for highly efficient heterogeneous photocatalyst to regulate electron structure of H_2-evolution active sites and improve their catalytic efficiency.

CRediT authorship contribution statement

Jiachao Xu: Methodology, Validation, Data curation, Writing – original draft. **Wei Zhong**: Investigation, Visualization. **Feng Chen**: Writing – review & editing. **Xuefei Wang:** Supervision, Project administration. **Huogen Yu:** Conceptualization, Resources, Funding acquisition, Writing – review & editing.

Declaration of Competing Interest

The authors declare that they have no known competing financial interests or personal relationships that could have appeared to influence the work reported in this paper.

Data Availability

Data will be made available on request.

Acknowledgments

This work was supported by the National Natural Science Foundation of China (U22A20147, 22075220 and 22178276) and the Natural Science Foundation of Hubei Province of China (2022CFA001).

Appendix A. Supporting information

Supplementary data associated with this article can be found in the online version at doi:10.1016/j.apcatb.2023.122493.

References

[1] R. Kawamura, N.T. Cuong, T. Fujita, R. Ishibiki, T. Hirabayashi, A. Yamaguchi, I. Matsuda, S. Okada, T. Kondo, M. Miyauchi, Photoinduced hydrogen release from hydrogen boride sheets, Nat. Commun. 10 (2019) 4880.
[2] Y. Guo, Q. Zhou, J. Nan, W. Shi, F. Cui, Y. Zhu, Perylenetetracarboxylic acid nanosheets with internal electric fields and anisotropic charge migration for photocatalytic hydrogen evolution, Nat. Commun. 13 (2022) 2067.
[3] D. Gao, J. Xu, L. Wang, B. Zhu, H. Yu, J. Yu, Optimizing atomic hydrogen desorption of sulfur-rich NiS_{1+x} cocatalyst for boosting photocatalytic H_2 evolution, Adv. Mater. 34 (2021) 2108475.
[4] Y. Chen, Q. Qiao, J. Cao, H. Li, Z. Bian, Precious metal recovery, Joule 5 (2021) 3097–3115.
[5] J. Wang, J. Chen, P. Wang, J. Hou, C. Wang, Y. Ao, Robust photocatalytic hydrogen evolution over amorphous ruthenium phosphide quantum dots modified g-C_3N_4 nanosheet, Appl. Catal. B: Environ. 239 (2018) 578–585.
[6] Z. Huang, Q. Zhou, J. Wang, Y. Yu, Fermi-level-tuned MOF-derived N-ZnO@NC for photocatalysis: a key role of pyridine-N-Zn bond, J. Mater. Sci. Technol. 112 (2022) 68–76.
[7] X. Hong, X. Yu, L. Wang, Q. Liu, J. Sun, H. Tang, Lattice-matched CoP/CoS_2 heterostructure cocatalyst to boost photocatalytic H_2 generation, Inorg. Chem. 60 (2021) 12506–12516.
[8] X. Yue, J. Fan, Q. Xiang, Internal electric field on steering charge migration: modulations, determinations and energy-related applications, Adv. Funct. Mater. 32 (2021) 2110258.
[9] Y. Lu, X. Ou, W. Wang, J. Fan, K. Lv, Fabrication of TiO_2 nanofiber assembly from nanosheets (TiO_2-NFs-NSs) by electrospinning-hydrothermal method for improved photoreactivity, Chin. J. Catal. 41 (2020) 209–218.
[10] J. Xu, W. Zhong, D. Gao, X. Wang, P. Wang, H. Yu, Phosphorus-enriched platinum diphosphide nanodots as a highly efficient cocatalyst for photocatalytic H_2 evolution of CdS, Chem. Eng. J. 439 (2022), 135758.
[11] C. Du, S. He, Y. Xing, Q. Zhao, C. Yu, X. Su, J. Feng, J. Sun, S. Dong, Fabricating S-scheme BiOBr/$Zn_2In_2S_5$ heterojunction for synergistic adsorption-photocatalytic degradation of tetracycline, Mater. Today Phys. 27 (2022), 100827.
[12] J. He, L. Hu, C. Shao, S. Jiang, C. Sun, S. Song, Photocatalytic H_2O overall splitting into H_2 bubbles by single atomic sulfur vacancy CdS with spin polarization electric field, ACS Nano 15 (2021) 18006–18013.
[13] Y. Sheng, W. Li, L. Xu, Y. Zhu, High photocatalytic oxygen evolution via strong built-in electric field induced by high crystallinity of perylene imide supramolecule, Adv. Mater. 34 (2022) 2102354.
[14] F. Li, Y. Liu, Q. Chen, X. Gu, W. Dong, D. Zhang, H. Huang, B. Mao, Z. Kang, W. Shi, Transient photovoltage study of the kinetics and synergy of electron/hole co-extraction in MoS_2/Ag-In-Zn-S/carbon dot photocatalysts for promoted hydrogen production, Chem. Eng. J. 439 (2022), 135759.
[15] B. Qiu, M. Du, Y. Ma, Q. Zhu, M. Xing, J. Zhang, Integration of redox cocatalysts for artificial photosynthesis, Energy Environ. Sci. 14 (2021) 5260–5288.
[16] W. Wang, S. Zhu, Y. Cao, Y. Tao, X. Li, D. Pan, D.L. Phillips, D. Zhang, M. Chen, G. Li, H. Li, Edge-enriched ultrathin MoS_2 embedded yolk-shell TiO_2 with boosted charge transfer for superior photocatalytic H_2 evolution, Adv. Funct. Mater. 29 (2019) 1901958.
[17] D. Gao, H. Long, X. Wang, J. Yu, H. Yu, Tailoring antibonding-orbital occupancy state of selenium in Se-enriched $ReSe_{2+x}$ cocatalyst for exceptional H_2 evolution of TiO_2 photocatalyst, Adv. Funct. Mater. 33 (2023) 2209994.
[18] Z. Jiang, Q. Chen, Q. Zheng, R. Shen, P. Zhang, X. Li, Constructing 1D/2D Schottky-based heterojunctions between $Mn_{0.2}Cd_{0.8}S$ nanorods and Ti_3C_2 nanosheets for boosted photocatalytic H_2 evolution, Acta Phys. - Chim. Sin. 37 (2020) 2010059.
[19] K. Feng, J. Xu, Y. Chen, S. Li, Z. Kang, J. Zhong, Positively charged Pt-based nanoreactor for efficient and stable hydrogen evolution, Adv. Sci. 9 (2022) 2203199.

[20] J. Xu, D. Gao, H. Yu, P. Wang, B. Zhu, L. Wang, J. Fan, Palladium-copper nanodot as novel H_2-evolution cocatalyst: optimizing interfacial hydrogen desorption for highly efficient photocatalytic activity, Chin. J. Catal. 43 (2022) 215–225.

[21] D.P. Kumar, J. Choi, S. Hong, D.A. Reddy, S. Lee, T.K. Kim, Rational synthesis of metal-organic framework-derived noble metal-free nickel phosphide nanoparticles as a highly efficient cocatalyst for photocatalytic hydrogen evolution, ACS Sustain. Chem. Eng. 4 (2016) 7158–7166.

[22] P. Wang, Y. Mao, L. Li, Z. Shen, X. Luo, K. Wu, P. An, H. Wang, L. Su, Y. Li, S. Zhan, Unraveling the interfacial charge migration pathway at the atomic level in a highly efficient Z-scheme photocatalyst, Angew. Chem. Int. Ed. 58 (2019) 11329–11334.

[23] S. Tao, W. Zhong, Y. Chen, F. Chen, P. Wang, H. Yu, Bifunctional thioacetamide-mediated synthesis of few-layered $MoOS_x$ nanosheet-modified CdS hollow spheres for efficient photocatalytic H_2 production, Catal. Sci. Technol. 12 (2022) 6006–6015.

[24] P. Ganguly, M. Harb, Z. Cao, L. Cavallo, A. Breen, S. Dervin, D.D. Dionysiou, S. C. Pillai, 2D nanomaterials for photocatalytic hydrogen production, ACS Energy Lett. 4 (2019) 1687–1709.

[25] Y.-Y. Han, X.-L. Lu, S.-F. Tang, X.-P. Yin, Z.-W. Wei, T.-B. Lu, Metal-Free 2D/2D heterojunction of graphitic carbon nitride/graphdiyne for improving the hole mobility of graphitic carbon nitride, Adv. Energy Mater. 8 (2018) 1702992.

[26] D.B. Sulas-Kern, E.M. Miller, J.L. Blackburn, Photoinduced charge transfer in transition metal dichalcogenide heterojunctions-towards next generation energy technologies, Energy Environ. Sci. 13 (2020) 2684–2740.

[27] D. Gao, J. Xu, F. Chen, P. Wang, H. Yu, Unsaturated selenium-enriched $MoSe_{2+x}$ amorphous nanoclusters: one-step photoinduced co-reduction route and its boosted photocatalytic H_2-evolution activity for TiO_2, Appl. Catal. B: Environ. 305 (2022), 121053.

[28] T. Su, Q. Shao, Z. Qin, Z. Guo, Z. Wu, Role of interfaces in two-dimensional photocatalyst for water splitting, ACS Catal. 8 (2018) 2253–2276.

[29] D.A. Reddy, E.H. Kim, M. Gopannagari, Y. Kim, D.P. Kumar, T.K. Kim, Few layered black phosphorus/MoS_2 nanohybrid: a promising co-catalyst for solar driven hydrogen evolution, Appl. Catal. B: Environ. 241 (2019) 491–498.

[30] Q. Zhang, S. Huang, J. Deng, D.T. Gangadharan, F. Yang, Z. Xu, G. Giorgi, M. Palummo, M. Chaker, D. Ma, Ice-assisted synthesis of black phosphorus nanosheets as a metal-free photocatalyst: 2D/2D heterostructure for broadband H_2 evolution, Adv. Funct. Mater. 29 (2019) 1902486.

[31] J. Su, G.D. Li, X.H. Li, J.S. Chen, 2D/2D heterojunctions for catalysis, Adv. Sci. 6 (2019) 1801702.

[32] J. Mei, T. Liao, Z. Sun, 2D/2D heterostructures: rational design for advanced batteries and electrocatalysis, Energy Environ. Mater. 5 (2021) 115–132.

[33] X. Li, Y. Chen, Y. Tao, L. Shen, Z. Xu, Z. Bian, H. Li, Challenges of photocatalysis and their coping strategies, Chem. Catal. 2 (2022) 1315–1345.

[34] M. Shao, Y. Shao, J. Chai, Y. Qu, M. Yang, Z. Wang, M. Yang, W.F. Ip, C.T. Kwok, X. Shi, Z. Lu, S. Wang, X. Wang, H. Pan, Synergistic effect of 2D Ti_2C and g-C_3N_4 for efficient photocatalytic hydrogen production, J. Mater. Chem. A 5 (2017) 16748–16756.

[35] M. Zhu, S. Kim, L. Mao, M. Fujitsuka, J. Zhang, X. Wang, T. Majima, Metal-free photocatalyst for H_2 evolution in visible to near-infrared region: black phosphorus/graphitic carbon nitride, J. Am. Chem. Soc. 139 (2017) 13234–13242.

[36] Y.J. Yuan, D.Q. Chen, Y.W. Huang, Z.T. Yu, J.S. Zhong, T.T. Chen, W.G. Tu, Z. J. Guan, D.P. Cao, Z.G. Zou, MoS_2 nanosheet-modified $CuInS_2$ photocatalyst for visible-light-driven hydrogen production from water, ChemSusChem 9 (2016) 1003–1009.

[37] Y. Zhao, C. Shao, Z. Lin, S. Jiang, S. Song, Low-energy facets on CdS allomorph junctions with optimal phase ratio to boost charge directional transfer for photocatalytic H_2 fuel evolution, Small 16 (2020) 2000944.

[38] J. Li, G. Zhan, Y. Yu, L. Zhang, Superior visible light hydrogen evolution of janus bilayer junctions via atomic-level charge flow steering, Nat. Commun. 7 (2016) 11480.

[39] W. Zhong, B. Zhao, H. Yu, J. Fan, Simultaneously optimizing the number and efficiency of active Se sites in Se-rich a-$MoSe_x$ nanodot cocatalysts for efficient photocatalytic H_2, Evol., Sol. RRL 6 (2022) 2100832.

[40] L. Li, D. Yu, P. Li, H. Huang, D. Xie, C.-C. Lin, F. Hu, H.-Y. Chen, S. Peng, Interfacial electronic coupling of ultrathin transition-metal hydroxide nanosheets with layered MXenes as a new prototype for platinum-like hydrogen evolution, Energy Environ. Sci. 14 (2021) 6419–6427.

[41] Y. Chen, W. Zhong, F. Chen, P. Wang, J. Fan, H. Yu, Photoinduced self-stability mechanism of CdS photocatalyst: the dependence of photocorrosion and H_2-evolution performance, J. Mater. Sci. Technol. 121 (2022) 19–27.

[42] D.H. Kerridge, S.J. Walker, Molten potassium thiocyanate: the reactions of some compounds of molybdenum, rhodium and silver, J. Inorg. Nucl. Chem. 39 (1977) 1579–1581.

[43] D.H. Kerridge, N. Carthey, M. Hassanein, A.E. Eid, Thermogravimetric and spectroscopic studies on Trans-$[Co(en)_2Cl_2]Cl$ and Cis-$[Co(en)_2(NCS)Cl]ClO_4$ in Molten KSCN and $ZnCl_2$-KCl Eutectic, Thermochim. Acta 55 (1982) 327–332.

[44] H. Ou, P. Yang, L. Lin, M. Anpo, X. Wang, Carbon nitride aerogels for the photoredox conversion of water, Angew. Chem., Int. Ed. 56 (2017) 10905–10910.

[45] W. Zhong, D. Gao, P. Wang, X. Wang, H. Yu, Accelerating hydroxyl desorption by swapping catalytic sites in $RuMoS_{2+x}$ cocatalysts for efficient alkaline photocatalytic H_2 production, Appl. Catal. B: Environ. 319 (2022), 121910.

[46] G. Ghimire, K.P. Dhakal, W. Choi, Y.A. Esthete, S.J. Kim, T.T. Tran, H. Lee, H. Yang, D.L. Duong, Y.M. Kim, J. Kim, Doping-mediated lattice engineering of monolayer ReS_2 for modulating in-plane anisotropy of optical and transport properties, ACS Nano 17 (2021) 13770–13780.

[47] Q. Zhang, L. Fu, Novel insights and perspectives into weakly coupled ReS_2 toward emerging applications, Chem 5 (2019) 505–525.

[48] Y. Lv, W. Lei, S. Liu, W.H. Zhang, Nanosized ReS_2 monolayers embedded in nitrogen-doped carbon nanotubes for high-rate capacitive lithium storage, Adv. Electron. Mater. 5 (2019) 1800830.

[49] S. Liu, W. Lei, Y. Liu, Q. Qiao, W.H. Zhang, Hierarchical nanosheet-based MS_2 (M = Re, Mo, W) nanotubes prepared by templating sacrificial Te nanowires with superior lithium and sodium storage capacity, ACS Appl. Mater. Interfaces 10 (2018) 37445–37452.

[50] F. Lai, N. Chen, X. Ye, G. He, W. Zong, K.B. Holt, B. Pan, I.P. Parkin, T. Liu, R. Chen, Refining energy levels in ReS_2 nanosheets by low-valent transition-metal doping for dual-boosted electrochemical ammonia/hydrogen production, Adv. Funct. Mater. 30 (2020) 1907376.

[51] Z. Mei, G. Wang, S. Yan, J. Wang, Rapid microwave-assisted synthesis of 2D/1D $ZnIn_2S_4/TiO_2$ S-scheme heterojunction for catalyzing photocatalytic hydrogen evolution, Acta Phys. - Chim. Sin. 37 (2020) 2009097.

[52] M. Xiao-Wei, L. Hai-Feng, L. Yan-Yan, W. Lei, P. Xi-Peng, Y. Xiu-Jie, Dramatically enhanced visible-light-responsive H_2 evolution of $Cd_{1-x}Zn_xS$ via the synergistic effect of Ni_2P and 1T/2H MoS_2 cocatalysts, Chin. J. Struct. Chem. 40 (2021) 7–22.

[53] Y. Wang, C. Zeng, Y. Zhang, R. Su, D. Yang, Z. Wang, Y. Wu, H. Pan, W. Zhu, W. Hu, H. Liu, R. Yang, Promoted photocarriers separation by straining in 2D/2D van der Waals heterostructures for high-efficiency visible-light photocatalysis, Mater. Today Phys. 22 (2022), 100600.

[54] A.R. Puente Santiago, T. He, O. Eraso, M.A. Ahsan, A.N. Nair, V.S.N. Chava, T. Zheng, S. Pilla, O. Fernandez-Delgado, A. Du, S.T. Sreenivasan, L. Echegoyen, Tailoring the interfacial interactions of van der Waals 1T-MoS_2/C_{60} heterostructures for high-performance hydrogen evolution reaction electrocatalysis, J. Am. Chem. Soc. 142 (2020) 17923–17927.

[55] D. Wu, Q. Liang, H. Si, X. Yan, H. Huang, Z. Li, Z. Kang, Self-assembly of a heterogeneous microreactor with carbon dots embedded in Ti-MOF derived $ZnIn_2S_4/TiO_2$ microcapsules for efficient CO_2 photoreduction, J. Mater. Chem. A 10 (2022) 24519–24528.

[56] Y. Men, Y. Tan, P. Li, X. Cao, S. Jia, J. Wang, S. Chen, W. Luo, Tailoring the 3d-orbital electron filling degree of metal center to boost alkaline hydrogen evolution electrocatalysis, Appl. Catal. B: Environ. 284 (2021), 119718.

[57] W. Zhong, B. Zhao, X. Wang, P. Wang, H. Yu, Synchronously enhancing water adsorption and strengthening Se-Hads bonds in Se-Rich $RuSe_{2+x}$ cocatalyst for efficient alkaline photocatalytic H_2 production, ACS Catal. 13 (2023) 749–756.

[58] Q. Xu, L. Zhang, B. Cheng, J. Fan, J. Yu, S-scheme heterojunction photocatalyst, Chem 6 (2020) 1543–1559.

[59] Y. Chen, L. Li, Q. Xu, T. Düren, J. Fan, D. Ma, Controllable synthesis of g-C_3N_4 inverse opal photocatalysts for superior hydrogen evolution, Acta Phys. Chim. Sin. 37 (2020) 2009080.